Calculation of large-aspect-ratio tokamak and toroidally-averaged stellarator equilibria of high-beta reduced magnetohydrodynamics via simulated annealing

M. Furukawa, Takahiro Watanabe, P. J. Morrison, and K. Ichiguchi

Citation: Physics of Plasmas **25**, 082506 (2018); doi: 10.1063/1.5038043
View online: https://doi.org/10.1063/1.5038043
View Table of Contents: http://aip.scitation.org/toc/php/25/8
Published by the American Institute of Physics

PHYSICS OF PLASMAS **25**, 082506 (2018)

Calculation of large-aspect-ratio tokamak and toroidally-averaged stellarator equilibria of high-beta reduced magnetohydrodynamics via simulated annealing

M. Furukawa,[1,a)] Takahiro Watanabe,[1] P. J. Morrison,[2] and K. Ichiguchi[3,4]
[1]*Faculty of Engineering, Tottori University, Minami 4-101, Koyama-cho, Tottori-shi, Tottori 680-8552, Japan*
[2]*Physics Department and Institute for Fusion Studies, University of Texas at Austin, Austin, Texas 78712, USA*
[3]*National Institute for Fusion Science, 322-6 Oroshi-cho, Toki 509-5292, Japan*
[4]*SOKENDAI, The Graduate University for Advanced Studies, Toki 509-5292, Japan*

(Received 30 April 2018; accepted 16 July 2018; published online 6 August 2018)

A simulated annealing (SA) relaxation method is used for the calculation of high-beta reduced magnetohydrodynamics (MHD) equilibria in toroidal geometry. The SA method, based on artificial dynamics derived from the MHD Hamiltonian structure, is used to calculate equilibria of large-aspect-ratio and circular-cross-section tokamaks as well as toroidally averaged stellarators. Tokamak equilibria including incompressible poloidal rotations are obtained and the Shafranov shift is seen to increase nearly quadratically in the rotation speed. A mapping procedure between non-rotating and poloidally rotating equilibria is shown to explain the quadratic dependence of equilibria shift on rotation. Calculated stellarator equilibria are seen to agree reasonably with previous results. The numerical results demonstrate the first successful application of the SA method to obtain toroidal equilibria. *Published by AIP Publishing*. https://doi.org/10.1063/1.5038043

I. INTRODUCTION

The calculation of magnetohydrodynamics (MHD) equilibria is an indispensable element of basic plasma physics, as well as the application to magnetic fusion research. Many methods for equilibrium calculations have been developed for two-dimensional and three-dimensional toroidal plasmas. The present work utilizes and develops the alternative simulated annealing (SA) method of Ref. 1 for the calculation of equilibria. This method is based on the fact that ideal fluid dynamics, including ideal MHD, possesses a Hamiltonian form in terms of a noncanonical Poisson bracket.[2] Because of the Hamiltonian form, ideal MHD conserves the energy of the system and has so-called Casimir invariants that arise from degeneracy of the Poisson bracket. With the SA method, we solve an artificial dynamics that is derived so that the energy of the system changes monotonically while the Casimir invariants are preserved. Given that equilibria are obtained by extremizing the energy at fixed Casimir invariants,[3–5] we can obtain an MHD equilibrium by solving the artificial SA dynamics as an initial-value problem.

A SA method was first developed for two-dimensional neutral fluid flows.[6–8] The method was significantly generalized in Ref. 1 by developing several kinds of brackets that monotonically change the energy of the system while preserving the Casimir or other invariants of the original system. There, a symmetric bracket with the possibility of various effects such as smoothing through a symmetric kernel and the preservation of chosen constraints, ones not inherent in the original dynamics, was introduced by making use of a Dirac bracket, and the general use of such brackets for obtaining equilibria was termed as "simulated annealing."

The SA method was applied to low-beta reduced MHD[9] in Ref. 10, using the reduced MHD Hamiltonian structure of Refs. 11 and 12. Various equilibria were successfully obtained in a two-dimensional rectangular domain with periodic boundaries in both dimensions. Moreover, a method was developed for pre-adjusting values of the Casimir invariants of an initial condition for the SA.[13] More recently, low-beta reduced MHD equilibria in cylindrical geometry were calculated by SA, where the inside of the plasma was helically deformed, even including magnetic islands.[14] The symmetric bracket with a smoothing effect was adopted in these studies, demonstrating the usefulness of SA for the MHD equilibrium calculation. For an overview of structure and structure-preserving algorithms for plasma physics from much wider view point, including SA, we refer to Ref. 15.

In the present paper, SA is applied to calculate high-beta reduced MHD[16] equilibria in toroidal geometry, which is possible because high-beta reduced MHD is also a Hamiltonian system.[11] Large-aspect-ratio and circular-cross-section tokamaks as well as toroidally averaged stellarator equilibria are calculated. The results obtained take into account the effect of toroidicity, where a proper accounting of the Shafranov shift[17] is observed. We compare our numerical results with the previous studies and obtain reasonable agreement. For tokamak equilibria, we also include incompressible poloidal rotation. This highlights one of the advantages of the SA method. The results given here comprise a significant next step towards ultimate goal of calculating MHD equilibrium in fully toroidal geometry.

Furthermore, in the present paper, we use a mapping procedure between non-rotating and poloidally rotating equilibria for high-beta reduced MHD. This is an extension to high-beta reduced MHD of the low-beta reduced MHD map first given in Ref. 18, which is a special case of the

---

[a)] furukawa@tottori-u.ac.jp

generalization of Refs. 19 and 20. This map nicely explains how equilibria change with poloidal rotation.

This paper is organized as follows. In Sec. II, the theory of the SA is described for high-beta reduced MHD. Next, we will explain numerical schemes for solving the equations of the SA and the convergence criterion in Sec. III. Then, equilibria of tokamaks and toroidally averaged stellarators are presented in Sec. IV. The results include tokamak equilibria with poloidal rotation. There these numerical results are compared and contrasted with the previous studies. The mapping procedure is also presented in Sec. IV. Conclusions are given in Sec. V.

II. FORMULATION

A. High-beta reduced MHD and normalization

The high-beta reduced MHD equations[16] are given by

$$\frac{\partial U}{\partial t} = [U, \varphi] + [\psi, J] - \varepsilon \frac{\partial J}{\partial \zeta} + [P, h] =: f^1, \tag{1}$$

$$\frac{\partial \psi}{\partial t} = [\psi, \varphi] - \varepsilon \frac{\partial \varphi}{\partial \zeta} =: f^2, \tag{2}$$

$$\frac{\partial P}{\partial t} = [P, \varphi] =: f^3. \tag{3}$$

Here, the fluid velocity $\boldsymbol{v}$ and the magnetic field $\boldsymbol{B}$ are expressed by

$$\boldsymbol{v} = \hat{z} \times \nabla \varphi, \tag{4}$$

$$\boldsymbol{B} = \nabla \psi \times \hat{z} + \hat{z}, \tag{5}$$

where the unit vector in the toroidal direction is denoted by $\hat{z}$. A coordinate system (r, θ, ζ) is used, where r is the minor radius, θ is the poloidal angle, and ζ is the toroidal angle. The length in the toroidal direction is measured by $z := R_0 \zeta$ with R_0 being the major radius of the toroidal plasma and $x := r \cos \theta$. The stream function and the magnetic flux function are denoted by φ and ψ, respectively, with the vorticity in the ζ-direction defined by $U := \triangle_\perp \varphi$ and the current density in the negative ζ-direction defined by $J := \triangle_\perp \psi$. The two-dimensional gradient operator $\nabla_\perp$ is defined in the r–θ plane, and the corresponding Laplacian is defined as usual by $\triangle_\perp := \nabla_\perp \cdot \nabla_\perp$. The Poisson bracket between any functions f and g is defined by $[f, g] := \hat{z} \cdot \nabla f \times \nabla g$. Quantities appearing in the equations above are normalized by the plasma minor radius a, a typical mass density ρ_0, a typical pressure p_0, a toroidal magnetic field B_0, an Alfvén velocity defined by $v_A := B_0/\sqrt{\mu_0 \rho_0}$, where μ_0 is the vacuum permeability, and an Alfvén time defined by $\tau_A := a/v_A$. An inverse aspect ratio is defined by $\varepsilon := a/R_0$. Finally, $P := \beta_0 p$ with $\beta_0 := 2\mu_0 p_0 / B_0^2$ and p being the normalized pressure, and $h := \varepsilon x$. The right-hand sides f^1, f^2, and f^3 are defined for later use.

Note that if the ζ-derivative terms in Eqs. (1) and (2) are dropped, then the system reduces to axisymmetric dynamics. The effect of the toroidal geometry appears only through the last term of Eq. (1).

We also note that the reduced MHD equations (1)–(3) have the same form as the reduced MHD equations for helical plasmas derived under the stellarator expansion.[21] However, three changes of Eqs. (1)–(3) are needed for stellarators. First, the toroidal angle ζ is understood as a toroidal angle for long wavelength structures; short wavelength structures are averaged out in the toroidal direction. Second, the poloidal flux function ψ is replaced by a total poloidal flux function $\Psi := \Psi_h + \psi$, where Ψ_h is a helical flux generated by external coils. Third, the curvature term h is replaced by $\frac{1}{2}\Omega$, where Ω is the sum of the curvature of the toroidal magnetic field and that of the helical magnetic field. Details of Ψ_h and Ω will be given in Sec. IV C.

B. Hamiltonian formulation

For the high-beta reduced MHD equations, the Hamiltonian form was presented in Refs. 11 and 12. The Hamiltonian is given by

$$H[\boldsymbol{u}] := \int_{\mathcal{D}} \mathrm{d}^3 x \left(\frac{1}{2} |\nabla_\perp (\triangle_\perp^{-1} U)|^2 + \frac{1}{2} |\nabla_\perp \psi|^2 - hP \right), \tag{6}$$

where the state vector $\boldsymbol{u} := (U, \psi, P)^{\mathrm{T}}$ and the domain is denoted by $\mathcal{D}$.

The functional derivative of $H[\boldsymbol{u}]$ is defined through

$$\lim_{\delta \boldsymbol{u} \to 0} (H[\boldsymbol{u} + \delta \boldsymbol{u}] - H[\boldsymbol{u}]) = \int_{\mathcal{D}} \mathrm{d}^3 x \frac{\delta H[\boldsymbol{u}]}{\delta u^i} \delta u^i, \tag{7}$$

where $i = 1, 2, 3$ and we sum over the repeated indices. Then, $\delta H[\boldsymbol{u}]/\delta \boldsymbol{u}$ is obtained as

$$\frac{\delta H[\boldsymbol{u}]}{\delta \boldsymbol{u}} = \begin{pmatrix} -\varphi \\ -J \\ -h \end{pmatrix}. \tag{8}$$

By defining the Poisson operator as

$$\mathcal{J} := \begin{pmatrix} -[U, \circ] & -[\psi, \circ] + \varepsilon \dfrac{\partial}{\partial \zeta} & -[P, \circ] \\ -[\psi, \circ] + \varepsilon \dfrac{\partial}{\partial \zeta} & 0 & 0 \\ -[P, \circ] & 0 & 0 \end{pmatrix}, \tag{9}$$

high-beta reduced MHD can be written in Hamiltonian form as

$$\frac{\partial \boldsymbol{u}}{\partial t} = \mathcal{J} \frac{\delta H[\boldsymbol{u}]}{\delta \boldsymbol{u}} = \{\boldsymbol{u}, H\}, \tag{10}$$

where in the last equality the Poisson bracket is used. A general noncanonical Poisson bracket has the form

$$\{F, G\} := \int_{\mathcal{D}} \mathrm{d}^3 x' \int_{\mathcal{D}} \mathrm{d}^3 x'' \frac{\delta F[\boldsymbol{u}]}{\delta u^i(\boldsymbol{x}')} J^{ij}(\boldsymbol{x}', \boldsymbol{x}'') \frac{\delta G[\boldsymbol{u}]}{\delta u^j(\boldsymbol{x}'')}, \tag{11}$$

where J^{ij} denoting the components of a Poisson operator. In our case, $J = \delta^3(\boldsymbol{x}' - \boldsymbol{x}'')\mathcal{J}$, with $\mathcal{J}$ being given by Eq. (9). (See Ref. 5 for further details.)

C. Casimir invariant

A Casimir invariant is defined to be a functional $C[\boldsymbol{u}]$ that satisfies $\{C, F\} = 0$ for any functional $F[\boldsymbol{u}]$, where the curly bracket denotes a noncanonical (degenerate) Poisson bracket. It is easily shown that the high-beta reduced MHD bracket defined by (9) has the following three Casimir invariants:

$$C_{\mathrm{v}} := \int_{\mathcal{D}} \mathrm{d}^3x\, U, \tag{12}$$

$$C_{\mathrm{m}} := \int_{\mathcal{D}} \mathrm{d}^3x\, \psi, \tag{13}$$

$$C_{\mathrm{p}} := \int_{\mathcal{D}} \mathrm{d}^3x\, P. \tag{14}$$

D. Artificial dynamics for relaxation

In this paper, we adopt an artificial dynamics defined by the following double bracket:[1,15]

$$((F,G)) := \int_{\mathcal{D}} \mathrm{d}^3x' \int_{\mathcal{D}} \mathrm{d}^3x''\, \{F, u^i(\boldsymbol{x}')\} K_{ij}(\boldsymbol{x}', \boldsymbol{x}'') \{u^j(\boldsymbol{x}''), G\}\,, \tag{15}$$

defined for any functionals $F[\boldsymbol{u}]$ and $G[\boldsymbol{u}]$, where $i, j = 1, 2, 3$ and (K_{ij}) is a symmetric kernel with a definite sign. The curly bracket in Eq. (15) is, in general, any Poisson bracket of the form of (11). When we take (K_{ij}) as positive definite, then the energy of the system decreases monotonically by the artificial dynamics

$$\frac{\partial \boldsymbol{u}}{\partial t} = ((\boldsymbol{u}, H)). \tag{16}$$

For the case at hand, it is convenient to introduce the following artificial convection fields:

$$\tilde{\varphi}(\boldsymbol{x}) := -\int_{\mathcal{D}} \mathrm{d}^3x'\, K_{1i}(\boldsymbol{x}, \boldsymbol{x}') f^i(\boldsymbol{x}'), \tag{17}$$

$$\tilde{J}(\boldsymbol{x}) := -\int_{\mathcal{D}} \mathrm{d}^3x'\, K_{2i}(\boldsymbol{x}, \boldsymbol{x}') f^i(\boldsymbol{x}'), \tag{18}$$

$$\tilde{h}(\boldsymbol{x}) := -\int_{\mathcal{D}} \mathrm{d}^3x'\, K_{3i}(\boldsymbol{x}, \boldsymbol{x}') f^i(\boldsymbol{x}'), \tag{19}$$

in terms of which the artificial evolution of Eq. (16) can be written compactly as

$$\frac{\partial U}{\partial t} = [U, \tilde{\varphi}] + [\psi, \tilde{J}] - \varepsilon \frac{\partial \tilde{J}}{\partial \zeta} + [P, \tilde{h}] =: \tilde{f}^1, \tag{20}$$

$$\frac{\partial \psi}{\partial t} = [\psi, \tilde{\varphi}] - \varepsilon \frac{\partial \tilde{\varphi}}{\partial \zeta} =: \tilde{f}^2, \tag{21}$$

$$\frac{\partial P}{\partial t} = [P, \tilde{\varphi}] =: \tilde{f}^3. \tag{22}$$

As we see, the convection fields φ, J, and h of the original evolution equations (1)–(3) are replaced by the artificial convection fields $\tilde{\varphi}$, $\tilde{J}$, and $\tilde{h}$, respectively. The right-hand sides $\tilde{f}^1$, $\tilde{f}^2$, and $\tilde{f}^3$ are again defined for later use.

Finally, we explain the boundary conditions. We will use a Fourier mode expansion in the poloidal and toroidal directions. For the poloidal mode number $m = 0$ components, the radial derivatives are set to be zero at $r = 0$, for the other m components, their values are set to be zero. At the plasma edge, all the Fourier components are set to be zero.

III. NUMERICAL SCHEMES AND CONVERGENCE CRITERION

A. Numerical schemes

In addition to the Fourier mode expansion in θ and ζ, the numerical scheme we adopt for solving Eqs. (20)–(22) employs a second-order finite difference method in r. Here, we only consider axisymmetric configurations; consequently, the mode number n for ζ only takes the value 0. The second-order implicit Runge-Kutta method is used for the time stepping, which is time-reversal symmetric and symplectic. The implicit equation associated with this procedure is solved by the Newton–Raphson method that uses the generalized minimum residual (GMRES) method[22] implemented in the Jacobian-free form.

We assume that the symmetric kernel (K_{ij}) in Eq. (15) is diagonal, as in Ref. 14, and we choose each diagonal term to have the form $\alpha_i g(\boldsymbol{x}', \boldsymbol{x}'')$, where α_i is a constant and $g(\boldsymbol{x}', \boldsymbol{x}'')$ is the three-dimensional Green's function defined through the Poisson equation

$$\triangle g(\boldsymbol{x}, \boldsymbol{x}'') = -\delta^3(\boldsymbol{x} - \boldsymbol{x}''). \tag{23}$$

Here, the three-dimensional Laplacian is written as $\triangle$ and $\delta^3(\boldsymbol{x} - \boldsymbol{x}'')$ is the three-dimensional Dirac delta function. This choice of (K_{ij}) introduces a smoothing effect in all directions.

B. Convergence criterion

The code used for the present calculations evolves the Fourier components of U, ψ, and P. Thus, the right-hand side of the evolution equations (20)–(22) is also Fourier decomposed. We write the Fourier coefficients of $((\boldsymbol{u}, H))$, i.e., $\tilde{f}^i$ as $\tilde{f}^i_{mn}$, where m and n denote the poloidal and toroidal mode numbers, respectively. We also write the Fourier coefficients of f^i of the original evolution equations (1)–(3) as f^i_{mn}. Then, the convergence criterion is set such that the maximum absolute values among f^i_{mn} and $\tilde{f}^i_{mn}$ become smaller than a threshold value. We took 10^{-6}, or smaller in some cases, as the threshold value in the numerical results in this paper.

IV. NUMERICAL RESULTS

A. Axisymmetric tokamak equilibrium without rotation

Let us turn to our first example, the calculation of large-aspect-ratio, circular-cross-section tokamak equilibria using SA. The initial conditions are chosen to be cylindrically symmetric with the profiles of the safety factor q and the pressure p as plotted in Fig. 1. We take $P = \beta_0 p$ and consider three cases with $\beta_0 = 0.1\%$, 0.5%, and 1%. The rotation

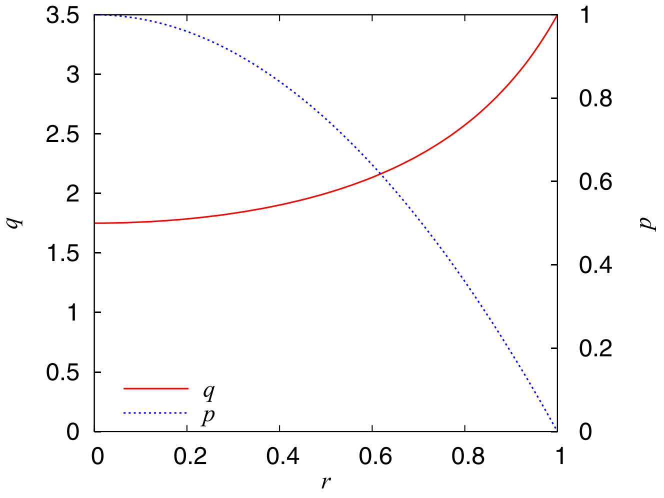

FIG. 1. The initial safety factor q and the pressure p profiles.

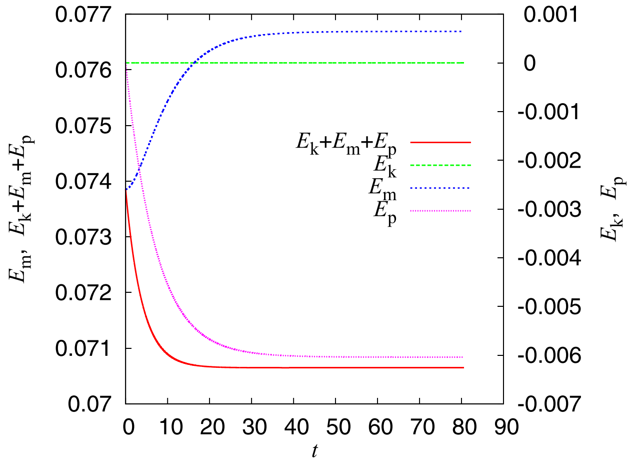

FIG. 2. Time evolution of the kinetic energy $E_{\rm k}$, the magnetic energy $E_{\rm m}$, the internal energy $E_{\rm p}$, and the total energy $E_{\rm k}+E_{\rm m}+E_{\rm p.}$ The magnetic energy increases as the time proceeds, while the internal energy decreases more, resulting in the total energy decreasing monotonically.

velocity is chosen to be zero and, consistently, the stream function $\varphi \equiv 0$. In Subsection IV B, we will consider the case of finite poloidal rotation. Throughout, the inverse aspect ratio is set to be $\varepsilon = 1/10$.

The time evolution of the total and various components of the energy is shown in Fig. 2 for the case of $\beta_0 = 1\%$. The kinetic, magnetic, and internal energies are denoted by $E_{\rm k}$, $E_{\rm m}$, and $E_{\rm p}$, respectively. The magnetic energy increases as the time proceeds, while the internal energy decreases with the total energy decreasing monotonically. Note that the kinetic energy remains zero, a consequence of $((U, H))$ being zero for the chosen initial condition, resulting in U remaining zero. Note that the time evolution for the cases $\beta_0 = 0.1\%$ and 0.5% is similar to those of Fig. 2. Also note that the Casimir invariants $C_{\rm v}$, $C_{\rm m}$, and $C_{\rm p}$ are well conserved in the simulation.

Figure 3 shows contour plots of ψ for the equilibria obtained in our three cases. The horizontal axis x is the distance along the major radius measured from the plasma center R_0. The vertical axis y is the height from the midplane. Observe, the Shafranov shift increases as β_0 is increased.

Figure 4 shows plots of the ψ profiles on the midplane of the three obtained equilibria, along with the initial ψ profile common to each case. As β_0 is increased, the peak of ψ moves outward. This is due to the increase in the $m = \pm 1$ and $n = 0$ components of ψ. For these numerical results, the $m = \pm 2$ and $n = 0$ components are very small for the inverse aspect ratio $\varepsilon = 1/10$. The pressure profiles also have the similar outward shift of their peaks.

From the peaks of the ψ profiles, we evaluated the Shafranov shift $\Delta(0)$, which is shown in Fig. 5. The result of our calculations denoted by "SA" is compared with the Shafranov shift obtained from the analytic solution using the large-aspect-ratio expansion,[23] denoted by "Shafranov eq.". In the latter, the Shafranov shift remains at $\beta_0 = 0$ since the toroidicity remains even at zero beta; however, the Shafranov shift seems to be zero at $\beta_0 = 0$ for SA. This is because the toroidal effect fully disappears at zero beta in high-beta reduced MHD.

We also note that ψ and P are convected by the same convection field $\tilde{\varphi}$ in the two-dimensional case. Therefore, the initial relation between ψ and P is retained, i.e., if we give an initial condition in a form $P = P(\psi)$, the same relation holds in the obtained equilibrium. This is shown in Fig. 6. We observe that the initial relation between ψ and P is retained for each β_0. This means, in a sense, that we can specify the pressure profile of the two-dimensional equilibrium to be obtained, as is usual when solving the Grad-Shafranov equation.

With SA, the total poloidal flux is conserved because of the Dirichlet boundary condition at the plasma edge. Therefore, the maximum value of ψ does not change from the initial condition, as we see in Fig. 6 as well as in Fig. 4. However, the safety factor profile changes from the initial condition. In tokamak equilibrium calculations, it may be necessary to control the safety factor profile. Such local profile control using SA will be a future issue.

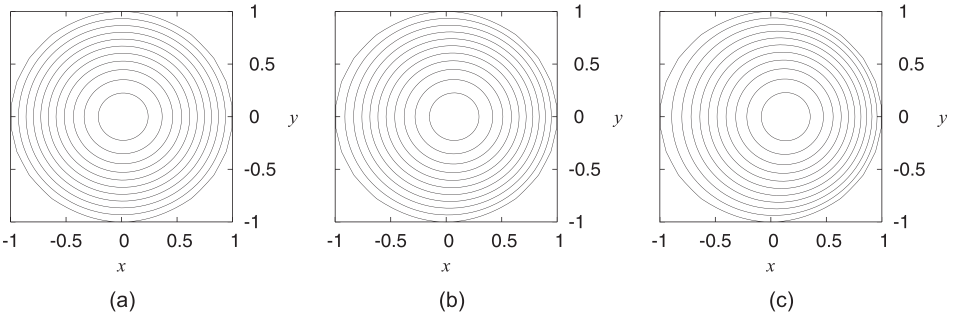

(a) (b) (c)

FIG. 3. Contour plots of ψ for (a) $\beta_0 = 0.1\%$, (b) 0.5%, and (c) 1%. The horizontal axis x denotes the distance along the major radius direction measured from the center of the plasma R_0. The vertical axis y is the height from the midplane.

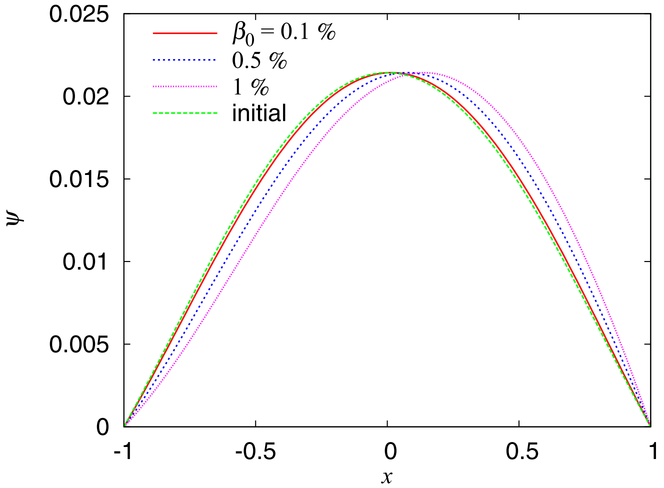

FIG. 4. The ψ profiles on the midplane for three equilibria obtained by simulated annealing, along with the initial ψ profile common to each case.

B. Axisymmetric tokamak equilibrium with poloidal rotation

One of the advantages of SA is that it can handle various types of plasma rotation. Substantial literature exists for axisymmetric tokamak equilibria with plasma rotations and we mention Refs. 24–27 as examples, and there are recent results on a numerical code for equilibrium calculations of two-fluid equations,[28] where both toroidal and poloidal rotations can exist in the equilibrium. In the present model, the rotation is in the poloidal direction. Note that the purely poloidal rotation is possible only in the large aspect ratio limit, under which the reduced MHD model is derived. Because the flow is incompressible, there is no difficulty in calculating such equilibria. We performed SA starting from the same initial conditions in Subsection IV A for ψ and P, but now we choose a φ that gives $v_\theta = 4 v_{\theta \max} r(1-r)$. Therefore, v_θ has its maximum value $v_{\theta \max}$ at $r = 1/2$ when $t = 0$. The rotation profile can change as time proceeds. Indeed, φ must be a function of ψ in the equilibrium according to the Ohm's law (2) with axisymmetry. The flux surfaces shift outward in the major radius direction at finite beta, and thus φ must also change from the initial condition to meet the equilibrium condition. Figure 7 shows that the Shafranov shift of the magnetic axis $\Delta(0)$ increases approximately quadratically in the poloidal rotation speed. This is due to the dynamic pressure of the flow. Here, the poloidal rotation speed is normalized by the toroidal Alfvén velocity, but if we normalize it by the poloidal Alfvén velocity at the plasma edge, $v_\theta = 10^{-2}$ corresponds to 3.5% of the poloidal Alfvén velocity. The increase in the Shafranov shift is about 5%–7% compared to the non-rotating equilibrium at $v_{\theta \max} = 10^{-2}$; however, the flux surface shape does not change much.

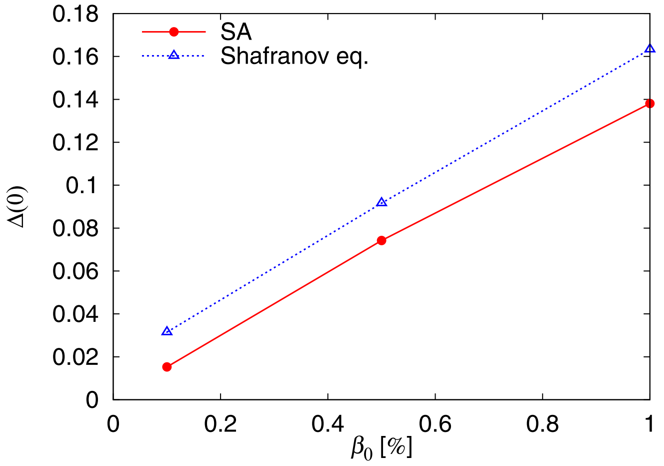

FIG. 5. The Shafranov shift $\Delta(0)$ vs. β_0. Here, "SA" denotes the simulated annealing result, while "Shafranov eq." denotes the analytic solution obtained by large-aspect-ratio expansion.

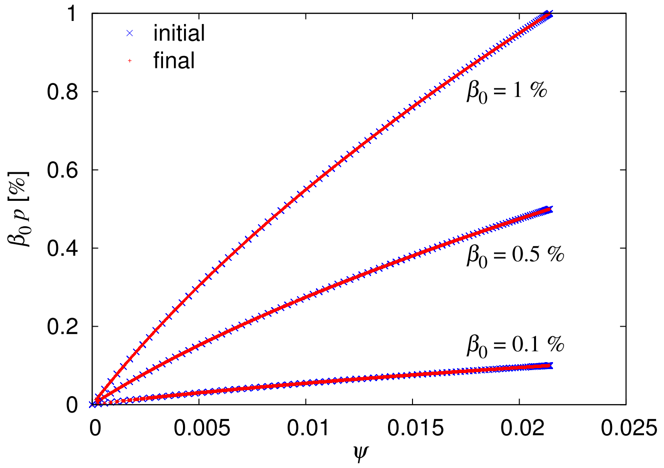

FIG. 6. The relation between ψ and $P = \beta_0 p$ is shown in a scatter plot using ψ and P at 10^4 points on the poloidal cross section. For each β_0, the initial relation between ψ and P is retained.

Here, we explain a mapping procedure between an equilibrium without rotation and poloidally rotating equilibria for the high-beta reduced MHD and then show that the quadratic dependence on the poloidal rotation speed can be explained by the map. The map is an extension of a map first derived for the low-beta reduced MHD in Ref. 18 and a special case of that of Refs. 19 and 20. The equilibrium equations including the poloidal rotation are given by $f^i = 0$ $(i = 1, 2, 3)$. From the equation for $i = 2$, or $[\psi, \varphi] = 0$, we obtain $\varphi = G(\psi)$, where G is an arbitrary function. Also from the

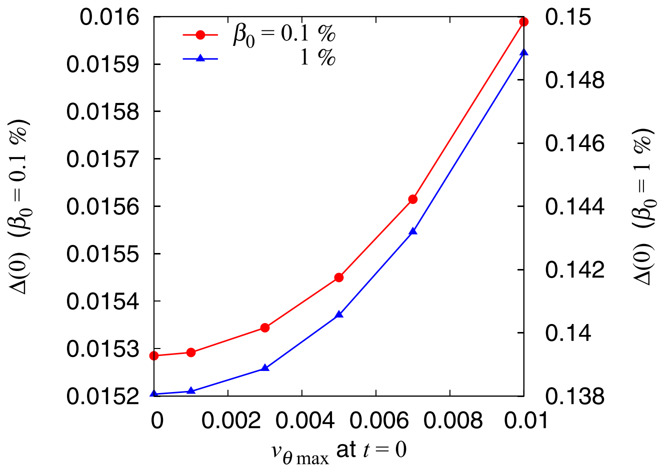

FIG. 7. The effect of poloidal rotation on the Shafranov shift for $\beta_0 = 0.1\%$ and 1%. The Shafranov shift increases quadratically in $v_{\theta \max}$.

equation for $i=3$, or $[P, \varphi]=0$, we obtain $P=K(\varphi) = K\circ G(\psi) =: L(\psi)$, where K is an arbitrary function. Noting that $J=\triangle_\perp \psi$ and

$$U=\triangle_\perp \varphi = G'(\psi)\triangle_\perp\psi + G''(\psi)|\nabla_\perp\psi|^2, \tag{24}$$

$f^1=0$ reads

$$\left[G'^2(\psi)\triangle_\perp\psi + G'(\psi)G''(\psi)|\nabla_\perp\psi|^2, \psi\right] - [\triangle_\perp\psi, \psi] - \left[hL'(\psi), \psi\right] = 0. \tag{25}$$

Therefore, we obtain[12]

$$(1-G'^2(\psi))\triangle_\perp\psi - G'(\psi)G''(\psi)|\nabla_\perp\psi|^2 + hL'(\psi) + F(\psi) = 0, \tag{26}$$

where $F(\psi)$ is an arbitrary function. This is an extended Grad-Shafranov equation for a poloidally rotating equilibrium. By setting $G(\psi)\equiv 0$, we obtain the Grad-Shafranov equation without rotation as

$$\triangle_\perp\psi + hL'(\psi) + F(\psi) = 0. \tag{27}$$

Now, if we define

$$\chi = X(\psi) := \int^\psi \sqrt{1-G'^2(\psi')}\,\mathrm{d}\psi', \tag{28}$$

the equilibrium equation can be rewritten as

$$\triangle_\perp\chi + h\bar{L}'(\chi) + \bar{F}(\chi) = 0, \tag{29}$$

where

$$\bar{L}'(\chi) := \frac{L'(X^{-1}(\chi))}{\sqrt{1-G'^2(X^{-1}(\chi))}}, \tag{30}$$

$$\bar{F}(\chi) := \frac{F(X^{-1}(\chi))}{\sqrt{1-G'^2(X^{-1}(\chi))}}. \tag{31}$$

Note that $X^{-1}(\chi)=\psi$. Equation (29) has the same form as Eq. (27) for an equilibrium without rotation. Therefore, an equilibrium without rotation can be mapped to equilibria with poloidal rotation. We see that the source terms of Eq. (29) are changed by the factor $1/\sqrt{1-G'^2(\psi)}$. Here, $G'(\psi)$ expresses the poloidal rotation velocity normalized by the poloidal Alfvén velocity. When $|G'^2(\psi)| \ll 1$, the factor can be approximated as $1/\sqrt{1-G'^2(\psi)} \simeq 1+\frac{1}{2}G'^2(\psi)$ that indicates effective increase in the source term, such as the pressure gradient, quadratically in the poloidal rotation speed. This explains the quadratic dependence of the Shafranov shift on the poloidal rotation speed. We also point out that any equilibria without rotation can be identified with one with rotation by a choice of G. This, of course, includes the equilibria obtained here by SA.

C. Heliotron equilibrium averaged over toroidal direction

For our next example, we consider heliotron equilibria averaged over the toroidal direction. As mentioned at the end of Sec. II A, the reduced MHD equations (1)–(3) can be used for stellarators under an appropriate replacement of variables. Here, we further assume that the dependence of the equilibrium quantities on ζ, the toroidal angle for the long wavelength structure, vanishes. Then, the ζ-derivative terms drop out.

The poloidal flux function ψ is replaced by a total poloidal flux function $\Psi := \Psi_{\mathrm{h}} + \psi$, where Ψ_{h} is independent of time. Thus, $\partial\Psi_{\mathrm{h}}/\partial t = 0$ and only ψ on the right-hand side needs to be replaced. The poloidal flux function due to helical coils, derived under the cylindrical approximation, is given in normalized form by

$$\Psi_{\mathrm{h}} := -\frac{\iota\!\!\!-_{\mathrm{h}}(a)}{M}\frac{F(M\varepsilon r)}{F'(M\varepsilon)}, \tag{32}$$

where $\iota\!\!\!-_{\mathrm{h}}(a)$ is a rotational transform generated by the helical coils, evaluated at the plasma edge, M is the pitch number, ε is the inverse aspect ratio, and

$$F(M\varepsilon r) := \frac{\ell}{M\varepsilon r} I_\ell(M\varepsilon r) I'_\ell(M\varepsilon r). \tag{33}$$

Here, ℓ is the pole number, $I_\ell(z)$ denotes the ℓ-th order modified Bessel function of the first kind, and $I'_\ell(z)$ denotes a z derivative of $I_\ell(z)$.

The curvature term Ω, derived under cylindrical approximation, is given in normalized form by

$$\Omega := 2\varepsilon r\cos\theta + \varepsilon\iota\!\!\!-_{\mathrm{h}}(a)\frac{G(M\varepsilon r)}{F'(M\varepsilon)}, \tag{34}$$

where $F'(M\varepsilon)$ denotes the derivative of F with respect to $M\varepsilon r$ and is evaluated at $r=1$, and

$$G(M\varepsilon r) := \left(I'_\ell(M\varepsilon r)\right)^2 + \frac{\ell^2 + (M\varepsilon r)^2}{(M\varepsilon r)^2}\left(I_\ell(M\varepsilon r)\right)^2. \tag{35}$$

The first and the second terms of Ω are the toroidal magnetic field curvature and the helical curvature, respectively.

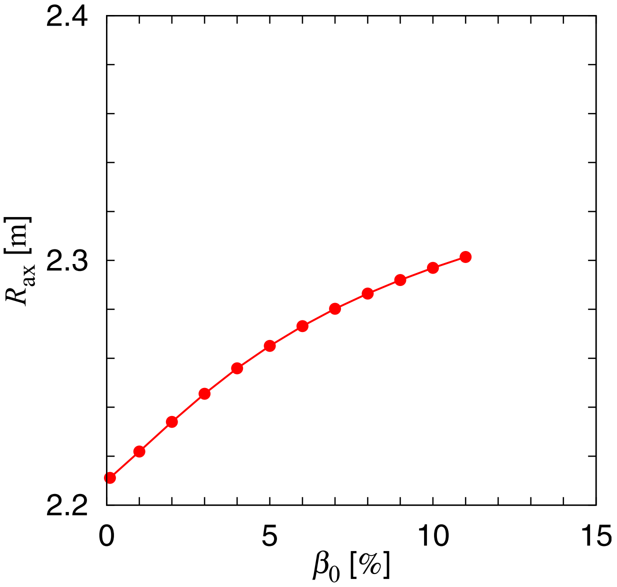

FIG. 8. The magnetic axis position R_{ax} plotted against β_0.

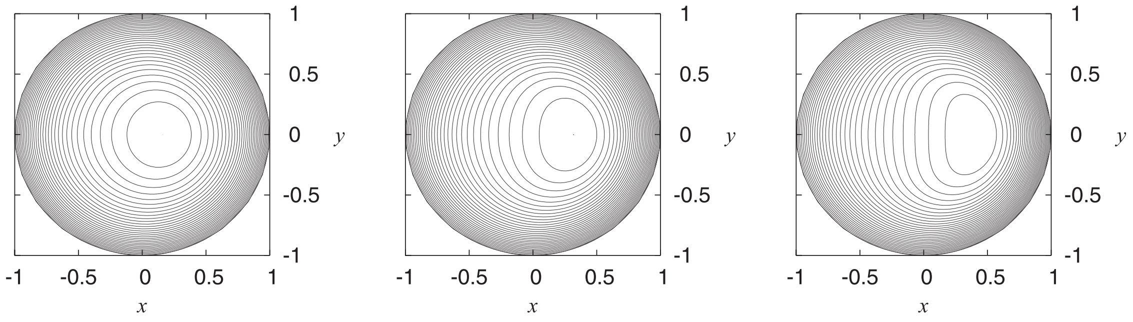

(a) (b) (c)

FIG. 9. Contour plots of Ψ for (a) $\beta_0 = 3\%$, (b) $\beta_0 = 7\%$, and (c) $\beta_0 = 11\%$.

We seek to reproduce simulations of the Heliotron E device published in Ref. 29. We assume the inverse aspect ratio $\varepsilon = 1/10$, which is similar to that of the Heliotron E device, and that the poloidal cross section has a circular shape. Also, we set the pole number $\ell = 2$ and the pitch number $M = 19$.

For the initial pressure profile, we take $P = \beta_0(1 - s)^2$ with $s := (\Psi - \Psi(0))/(\Psi(a) - \Psi(0))$ being a normalized total poloidal flux function, where $\Psi(0)$ and $\Psi(a)$ are evaluated at the magnetic axis and at the plasma edge, respectively. This is the same profile as that of Ref. 29. Note that this pressure profile remains unchanged during the artificial SA dynamics, as explained in the last part of Sec. IV A.

It is difficult to completely reproduce the results of Ref. 29 for several reasons. First, the net plasma current in the toroidal direction on each flux surface cannot be kept zero with the form of SA used here, while in Ref. 29 it is set to be zero. The second reason is that there is difficulty in controlling the local profile of the rotational transform $\iota\!\!\!-$ with SA. Because of these two reasons, we cannot perfectly match the rotational transform with that of Ref. 29. A third reason is that the expressions for the helical flux Ψ_h in Eq. (32) and the magnetic curvature Ω in Eq. (34) are derived under the cylindrical approximation, while those in Ref. 29 are calculated numerically from helical coil currents in toroidal geometry. The last reason is due to the difference of the shape of the plasma edge. In our simulation, it is exactly circular, while it is slightly elongated in Ref. 29. The aspect ratio is also not exactly matched. Despite these reasons, we observe reasonable agreement between our SA results and those of Ref. 29.

Figure 8 shows the magnetic axis position R_{ax} as a function of β_0. Observe that the tendency and the magnitude of the magnetic axis shift agree reasonably with Fig. 2(a) of Ref. 29, despite the differences explained above.

The shapes of the flux surfaces are shown in Fig. 9. A similar figure of flux surfaces is presented in Fig. 3 of Ref. 29 for $\beta_0 = 7\%$. The shapes of the flux surfaces in the central region of the plasma, especially the deformation to the D shape at high beta, show behavior similar to that of Ref. 29.

Figure 10 depicts the rotational transform. Here, in Fig. 10(a), the radial profiles of $\iota\!\!\!-$ for $\beta_0 = 3\%$, 7%, and 11% are plotted as functions of the normalized total poloidal flux s. Also $\iota\!\!\!-$ at the magnetic axis $\iota\!\!\!-(0)$, at its minimum $\iota\!\!\!-_{\mathrm{min}}$, and at the plasma edge $\iota\!\!\!-(a)$ as functions of β_0 are shown in Fig. 10(b). Although it is difficult to identify from the figure, $\iota\!\!\!-(a)$ slightly decreases and $\iota\!\!\!-(0)$ slightly increases as β_0 is increased. We do not observe a difference between $\iota\!\!\!-(0)$ and $\iota\!\!\!-_{\mathrm{min}}$, as was observed in Ref. 29. The main reason for this difference is that the net current free condition in the equilibria of Ref. 29 is not imposed in our equilibria. The difference

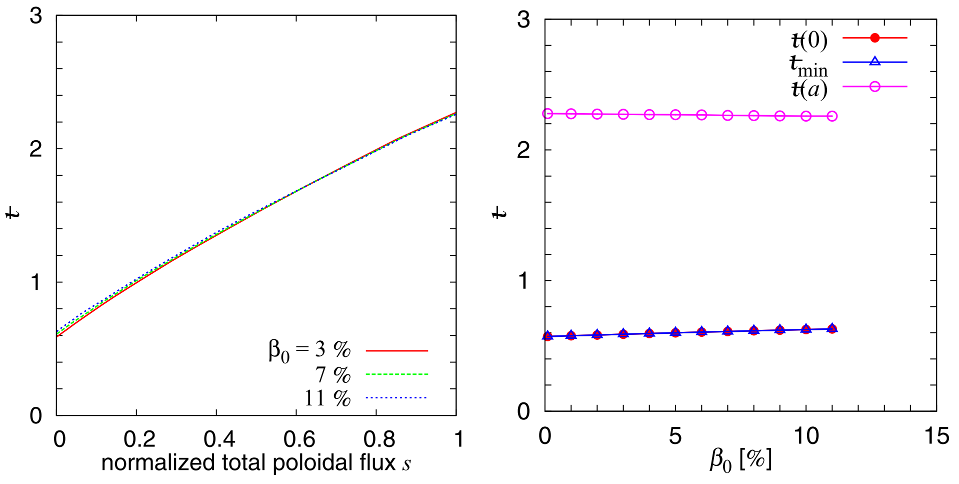

(a) (b)

FIG. 10. (a) The radial profiles of $\iota\!\!\!-$ for several values of β_0 as functions of the normalized total poloidal flux s. (b) The rotational transform at the magnetic axis $\iota\!\!\!-(0)$, at its minimum $\iota\!\!\!-_{\mathrm{min}}$, and at the plasma edge $\iota\!\!\!-(a)$ plotted against β_0.

between $\text{ɨ}(0)$ and $\text{ɨ}_{\rm min}$ arises because of the magnetic shear reversal that is caused by forcing the net zero current.

In summary, because of some differences in the equilibrium parameters, e.g., the net current, we do not obtain perfect agreement with Ref. 29. However, we obtain reasonable agreement, especially in the Shafranov shift and the flux surface shapes.

V. CONCLUSIONS

We have developed the theory of the simulated annealing for calculating high-beta reduced MHD equilibria in toroidal geometry. Large-aspect-ratio circular-cross section tokamak and toroidally averaged stellarator equilibria were successfully calculated. These equilibria possess the proper Shafranov shift according to the toroidal effect. We obtain reasonable agreement of our results with the previous studies. Especially for the tokamak equilibrium calculation, we obtained equilibria including poloidal rotation. For this case, the Shafranov shift of the magnetic axis increased quadratically in the poloidal rotation speed. The quadratic dependence is explained by the mapping procedure between nonrotating and poloidally rotating equilibria for high-beta reduced MHD. This achievement highlights one of the advantages of the simulated annealing method, i.e., it can handle equilibria with rotation.

ACKNOWLEDGMENTS

M.F. was supported by the JSPS KAKENHI Grant No. JP15K06647, while P.J.M. was supported by the U.S. Dept. of Energy Contract No. DE-FG05-80ET-53088. K.I. was supported by the budget NIFS17KLTT006 of the National Institute for Fusion Science and JSPS KAKENHI Grant No. 15k06651.

[1] G. R. Flierl and P. J. Morrison, Physica D **240**, 212 (2011).
[2] P. J. Morrison and J. M. Greene, Phys. Rev. Lett. **45**, 790 (1980).
[3] M. D. Kruskal and C. R. Oberman, Phys. Fluids **1**, 275 (1958).
[4] V. I. Arnol'd, Prikl. Math. Mech. **29**, 846 (1965), [J. Appl. Math. Mech. **29**, 1002–1008 (1965)].
[5] P. J. Morrison, Rev. Mod. Phys. **70**, 467 (1998).
[6] G. K. Vallis, G. F. Carnevale, and W. R. Young, J. Fluid Mech. **207**, 133 (1989).
[7] G. F. Carnevale and G. K. Vallis, J. Fluid Mech. **213**, 549 (1990).
[8] T. G. Shepherd, J. Fluid Mech. **213**, 573 (1990).
[9] H. R. Strauss, Phys. Fluids **19**, 134 (1976).
[10] Y. Chikasue and M. Furukawa, Phys. Plasmas **22**, 022511 (2015).
[11] P. J. Morrison and R. D. Hazeltine, Phys. Fluids **27**, 886 (1984).
[12] J. E. Marsden and P. J. Morrison, Contemp. Math. **28**, 133 (1984).
[13] Y. Chikasue and M. Furukawa, J. Fluid Mech. **774**, 443 (2015).
[14] M. Furukawa and P. J. Morrison, Plasma Phys. Controlled Fusion **59**, 054001 (2017).
[15] P. J. Morrison, Phys. Plasmas **24**, 055502 (2017).
[16] H. R. Strauss, Phys. Fluids **20**, 1354 (1977).
[17] V. D. Shafranov, Sov. Phys. - JETP **6**, 545 (1958).
[18] P. J. Morrison, Bull. Am. Phys. Soc. **31**, 1609 (1986).
[19] G. N. Throumoulopoulos and H. Tasso, J. Plasma Phys. **62**, 449 (1999).
[20] T. Andreussi, P. J. Morrison, and F. Pegoraro, Phys. Plasmas **19**, 052102 (2012).
[21] M. Wakatani, *Stellarator and Heliotron Devices* (Oxford Univ. Press, New York, Oxford, 1998).
[22] Y. Saad and M. H. Schultz, SIAM J. Sci. Stat. Comput. **7**, 856 (1986).
[23] V. D. Shafranov, in *Reviews of Plasma Physics*, edited by M. A. Leontovich (Consultants Bureau, New York, 1966), Vol. 2, p. 103.
[24] H. P. Zehrfeld and B. J. Green, Nucl. Fusion **12**, 569 (1972).
[25] B. J. Green and H. P. Zehrfeld, Nucl. Fusion **13**, 750 (1973).
[26] H. R. Strauss, Phys. Fluids **16**, 1377 (1973).
[27] E. Hameiri, Phys. Fluids **26**, 230 (1983).
[28] L. Guazzotto and R. Betti, Phys. Plasmas **22**, 092503 (2015).
[29] Y. Nakamura, M. Wakatani, and K. Ichiguchi, J. Plasma Fusion Res. **69**, 41 (1993).